

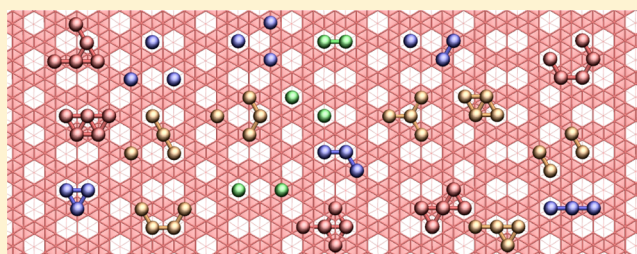
Polymorphism of Two-Dimensional Boron

Evgeni S. Penev, Somnath Bhowmick, Arta Sadrzadeh, and Boris I. Yakobson*

Department of Mechanical Engineering and Materials Science and Department of Chemistry, Rice University, Houston, Texas 77005, United States

ABSTRACT: The structural stability and diversity of elemental boron layers are evaluated by treating them as pseudoalloy $B_{1-x}\square_x$, where \square is a vacancy in the close-packed triangular B lattice. This approach allows for an elegant use of the cluster expansion method in combination with first-principles density-functional theory calculations, leading to a thorough exploration of the configurational space. A finite range of compositions x is found where the ground-state energy is essentially independent of x , uncovering a variety of stable B-layer phases (all metallic) and suggesting polymorphism, in stark contrast to graphene or hexagonal BN.

KEYWORDS: Boron layers, polymorphism, cluster expansion, density-functional theory



When it comes to its structural organization, elemental boron offers more puzzles than its close neighbors in the periodic table, ubiquitous carbon and silicon. On a large scale, boron displays multiple bulk phases,^{1,2} whereas its smallest clusters are also diverse, as established experimentally and in theory.^{3,4} For larger nanostructures, even their possibility and basic makeup remain unsettled. Two-dimensional (2D) layers, nanotubes, and fullerene-type cages yield very scarce factual evidence^{5–7} and remain a subject of ongoing debate. A recent prediction of the round boron molecule, the B_{80} buckyball,⁸ has ignited further interest. It was followed immediately by the proposals of stable 2D boron, particularly appealing as a graphene analog and called an α sheet.⁹ Inversely, the latter could be considered to be a precursor that can be folded into a B_{80} sphere or a nanotube.^{9–11}

The B_{80} buckyball remained a subject of particular interest in theory, in part because of its similarity to the celebrated C_{60} and also as being contested regarding its symmetry^{12,13} and stability relative to other proposed hollow, filled isomers or larger clusters.^{14–17} Although an overview of numerous clusters cannot be afforded here, one structure motivating the present study was a stable volleyball-shaped isomer.¹⁸ One could speculate that its planar development, unfolding into a 2D layer, may be rather stable as well. Direct computations indeed confirmed that this structure, dubbed here the $B(1/8)$ -layer,¹⁹ has cohesive energy as good as or even exceeding that of the established α -sheet [or $B(1/9)$ -sheet]. More importantly, it posed a broader question of the possible multiplicity of 2D structures of comparable stability and their coexistence in 2D formation. Because the layer serves as a building block for fullerenes,^{20,21} tubes,^{11,22} and nanoribbons,^{23–25} understanding the B layer's intrinsic patterns and stability is a prerequisite for all those nanostructures.²⁶

B layers are usually evaluated by density-functional theory (DFT) calculations^{9,27,28} for specific structures derived from a

close-packed triangular B layer (denoted B_{Δ} hereafter) by the selective removal of B atoms, a procedure that results in hexagonal voids or vacancies (\square). This leads to a very large number of possible configurations, exploring which poses a daunting combinatorial problem and hampers the direct use of first-principles methods. Hence, only a handful of B layers have been considered so far. Here we advance an approach to the structural diversity and stability of B layers based on the cluster expansion (CE) method²⁹ applied to the pseudoalloy system $B_{1-x}\square_x$. Vacancies in alloys can be treated routinely with the CE,^{30,31} and here we demonstrate that CE provides a route to the systematic first-principles study of B layers.

To map the problem of the B layers onto that of the $B_{1-x}\square_x$ pseudoalloy structure, we consider the full B_{Δ} as being composed of a honeycomb or kagome³² sublattice (B_{\square}) and a triangular sublattice defined by the hexagon centers (Figure 1, inset). The B_{\square} sublattice is configurationally inactive, but each site on the triangular sublattice can be either a B atom or a vacancy \square . The vacancy concentration is defined as $x = m/N$, where $m \in [0, n]$ ($n < N$) is the number of vacancies in a supercell of N lattice sites of B_{Δ} .^{9,33} To render various vacancy patterns, the rhombic 3×3 and $\sqrt{12} \times \sqrt{12}$ and rectangular $4 \times \sqrt{3}$ supercells can be initially employed (Figure 1).

The stability of various B layers can then be assessed in terms of their formation energy E_f . Any lattice configuration can be described by a vector $\sigma = \{\sigma_1, \sigma_2, \dots, \sigma_n\}$, with $\sigma_i = +1$ where the B atom is present and -1 if not (\square). Within the CE formalism, E_f for a particular configuration σ can be expressed as series²⁹

$$E_f(\sigma) = J_0 + (1 - 2x)J_1 + \sum_{\alpha} d_{\alpha} J_{\alpha} \bar{\Pi}_{\alpha}(\sigma) \quad (1)$$

Received: February 4, 2012

Revised: March 24, 2012

Published: April 11, 2012

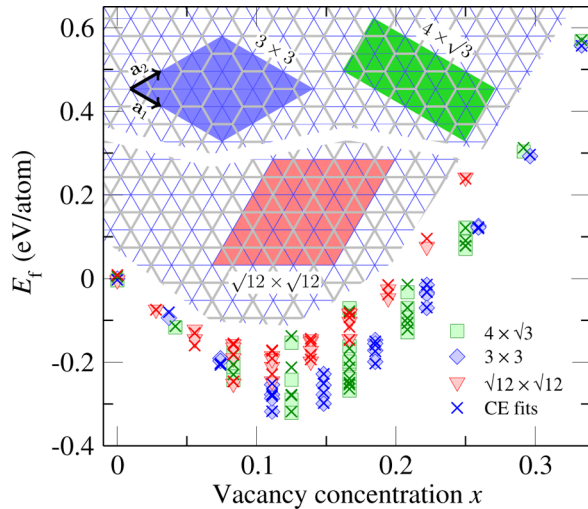


Figure 1. Formation energies E_f according to eq 2, along with the corresponding CE fits as a function of the vacancy concentration x in the $B_{1-x}O_x$ system. The supercells used are shown in the inset. The arrows indicate the lattice basis vectors; the fixed, configurationally inactive B_O sublattice is shown in gray.

where d_α is the number of clusters of type α (pairs, triplets, etc.), J_α is the corresponding effective cluster interaction, and $\bar{\Pi}_\alpha(\sigma) = \langle \prod_i \sigma_i \rangle$ represents the “spin” products for configuration σ averaged over all symmetry-equivalent α -type clusters. ATAT (alloy theoretical automated toolkit)³⁴ is used to determine the J_α expansion coefficients by fitting the energies to their direct DFT-computed values for all generated structures.

All DFT calculations were performed with the Quantum ESPRESSO package³⁵ using ultrasoft pseudopotentials in conjunction with the generalized gradient approximation to the electron exchange and correlation³⁶ and employing a plane-wave basis set with a 30 Ry kinetic energy cutoff. All B-layer geometries were represented by supercells (insets in Figures 1 and 3) with a 10 Å vacuum region in the normal direction. Summation over the Brillouin zone is carried out with a Monkhorst–Pack k -point set, ensuring approximately the same k -point density among different-sized supercells, using as a reference $4 \times 4 \times 1$ sampling for the 3×3 supercell (Figure 1). All structures were fully relaxed until the force on each atom (E_{tot} change in the self-consistency loop) was less than 10^{-3} Ry/Bohr (10^{-4} Ry).

For a supercell representing $B_{1-x}O_x$ at a given x , the formation energy is calculated from the total energy per atom of the supercell, $E_{\text{tot}}(x)$, relative to that of B_Δ

$$E_f(x) = E_{\text{tot}}(x) - E_{\text{tot}}(B_\Delta) \quad (2)$$

Figure 1 summarizes the DFT-calculated E_f and the CE fits; relevant supercell parameters are collected in Table 1. Note that the 2^n possible σ configurations are reduced by symmetry to reasonably small sets of $C_{\text{sym}} \leq 30$; therefore, one can exhaust all possibilities at the DFT level. As a standard measure of the CE quality, we use the cross-validation (CV) score³⁴ defined as

$$S_{\text{CV}}^2 = \frac{1}{M} \sum_i^M (E_i^{\text{DFT}} - E_i^{\text{CE}})^2 \quad (3)$$

where E_i^{CE} is fitted to the DFT-calculated formation energies of $M - 1$ other structures, excluding E_i^{DFT} . We have found that the

Table 1. Various Parameters of All Supercells Considered in the Present Work^a

supercell	N	n	C_{sym}	C_{DFT}	S_{CV}
$4 \times \sqrt{3}$	24	8	30	30	13.7
3×3	27	9	24	24	24.7
$\sqrt{12} \times \sqrt{12}$	36	9	24	24	24.9
4×4	48	16	528	46	7.2
$4 \times 2\sqrt{3}$	48	16	1369	50	5.9
$5 \times \sqrt{3}$	30	10	78	31	6.3

^a N , total number of sites; n , number of configurationally active sites; C_{sym} , total number of symmetry-inequivalent configurations; C_{DFT} , number of structures calculated with DFT; S_{CV} , cross-validation score (meV/atom) of the best CE fit.

inclusion of up to five-point clusters is necessary to obtain good-quality fits (Table 1). As an illustration, Figure 2 shows

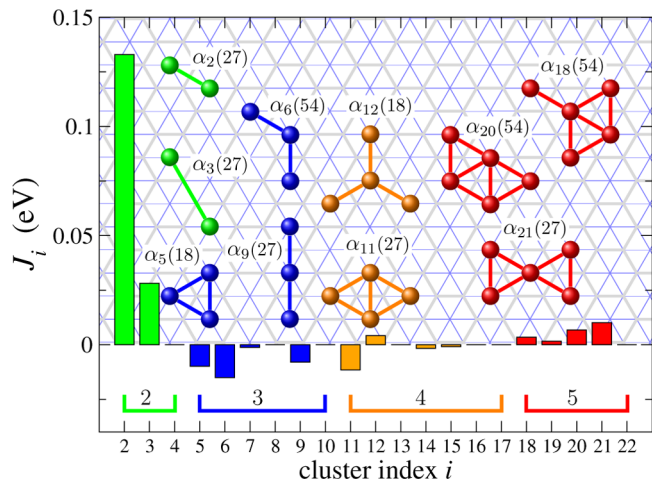


Figure 2. Effective cluster interactions J_i (excluding the empty and point clusters, $i = 0, 1$) for the 3×3 supercell (cf. Figure 1), fitted with ATAT.³⁴ The clusters α_i (“figures”) corresponding to the 10 strongest interactions are shown as ball-and-stick models, and the underlying grid represents the B_Δ lattice. Corresponding cluster multiplicities d_i (eq 1) are given in parentheses. The horizontal brackets group J ’s that correspond to the same cluster size $k = 2-5$.

the cluster geometries for the 3×3 supercell along with the magnitudes of the corresponding interactions. The dominant positive J values reflect the pairwise vacancy repulsion, whereas all nonvanishing three-point terms are attractive.

Not only does Figure 1 show agreement between the CE and DFT-computed energies and testify to the power of the CE method, but it also reveals the overall trend with the expressed minimum at around $x \approx 0.1-0.15$, where several most stable $B_{1-x}O_x$ structures are found (nearly degenerate in energy, within the computational accuracy). One is then compelled to explore this structural variability with the denser sampling that can be achieved by enlarging the supercells, as follows.

First, we note that in the range of interest and for higher x the $\sqrt{12} \times \sqrt{12}$ supercell based on the kagome lattice was the least efficient in detecting low-energy structures and can be omitted. In this case, any pair of nearest-neighbor vacancies results in an unfavorable four-fold bonding configuration of the shared B atom. On the basis of this observation, one can focus only on structures with a configurationally inactive honeycomb sublattice.

Accordingly, in the next step we enlarge the 3×3 to 4×4 and the $4 \times \sqrt{3}$ to $4 \times 2\sqrt{3}$ and $5 \times \sqrt{3}$ supercells (Figure 3

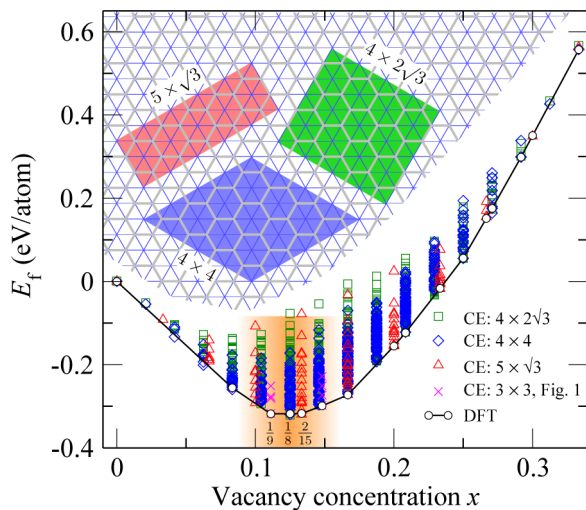


Figure 3. Formation energies E_f of all ≈ 2100 symmetry-inequivalent structures calculated from CE fits to ≈ 130 configurations calculated with DFT for the three supercells in the inset. Ground-state checking is carried out with ATAT³⁴ only over the range of $x \in [0.1, 0.15]$ (shaded region). For completeness, the values for the 3×3 supercell in this range of x (Figure 1) are also included. The exact fractions x that form a flat section of the DFT ground-state line are indicated as well.

and Table 1). Ideally, one would like to obtain the energies of larger supercells from eq 1 using the J values calculated from smaller ones. In practice, we found the S_{CV} to be rather high and it could not be improved any further because of the limited number of structures available for smaller supercells. We thus extended the DFT calculations to $C_{DFT} \approx 130$ selected structures, and the automated CE procedure³⁴ was run until very good CV scores were reached. The constructed CE's of eq 1 are then used to calculate the formation energies of all

enumerated symmetry-nonequivalent configurations for these supercells, and the results are shown in Figure 3.

This graph also reveals in greater detail the structural diversity of the stable B layers that, in fact, could already be anticipated from Figure 1. The CE is fully consistent with the DFT “ground-state line” (as obtained with ATAT) practically over the entire range of x although ground-state checking was explicitly requested only over the range indicated in Figure 3. The most stable configurations have $m = 3$ to 4 vacancies per $5 \times \sqrt{3}$ and 3×3 supercells and $m = 5$ –7 vacancies per 4×4 and $4 \times 2\sqrt{3}$ supercells, which correspond to the range $x \approx 0.1$ – 0.15 in $B_{1-x}\text{O}_x$. The distinguishing feature of the majority of these configurations is the presence of \square clusters. Remarkably, we uncover a finite range of $1/9 \leq x \leq 2/15$ where the DFT ground state line is flat, $E_f^{\text{DFT}}(x) = \text{const}$. At $x = 1/9$, it is straightforward to single out the most stable structure, the familiar α -sheet^{9,20} (Figure 4a) because this \square fraction is captured only by the relatively small 3×3 supercell (Figure 1). For the two slightly higher vacancy fractions, $x = 1/8$ and $2/15$ a considerable number of geometries are found whose formation energies are within a few meV/atom of the ground-state line. The corresponding lowest-energy geometries are given in Figure 4b,c, respectively.

It is evident from Figure 3 that any fraction x outside the 0.1 – 0.15 range results in less favorable configurations, with substantially increasing E_f . Here we focus only on flat geometries although out-of-plane atomic relaxations can have a stabilizing effect.^{6,33,37} However, such buckling is shown to be operative only for denser layers, at $x < 1/9$.³³ For the limiting case of B_{Δ} , we calculated that buckling indeed reduced $E_f(0)$ by 0.15 eV/atom. This suggests that accounting for layer buckling can lead to a less steep $E_f(x)$ line at $x \lesssim 1/9$ but will not affect the most stable ordered configurations. For the lowest-energy configurations with $x = 1/9$, $1/8$, and $2/15$ (Figure 3), we have verified that they are stable against several normal-to-the-plane atomic displacement patterns.

To rationalize the $B_{1-x}\text{O}_x$ stability, we analyze the electronic spectrum, viz., the projected density of states $D_i(E)$ of the best structures in the range of 0.1 – 0.15 (Figure 4). Clearly, all of

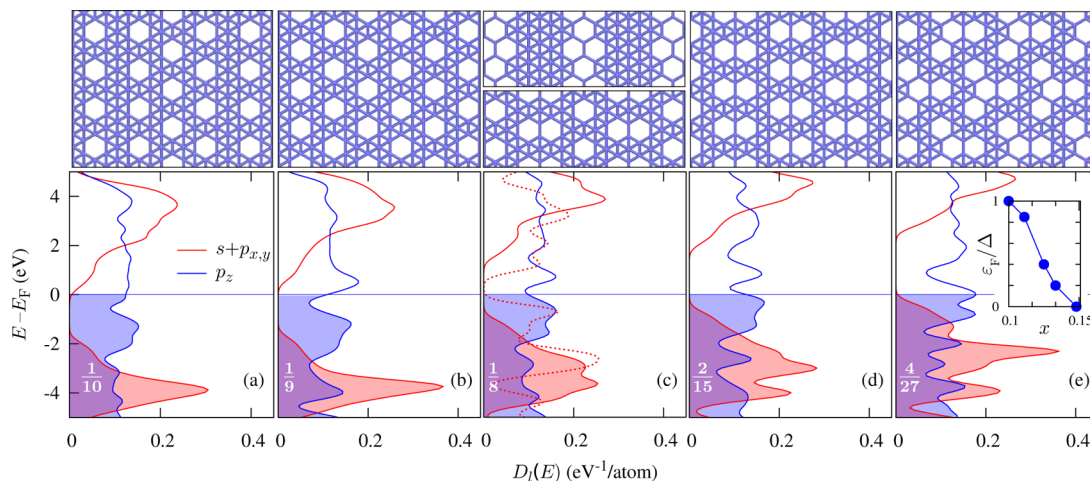


Figure 4. Projected density of states $D_i(E)$ (calculated using a finer \mathbf{k} mesh and 0.3 eV Gaussian broadening) for some of the most stable B layers in the range of $x \approx 0.1$ – 0.15 (exact x is indicated in the lower left corner). The corresponding patterns are shown above each. (b) The familiar α sheet.⁹ (c) The ground-state structure for $x = 1/8$ is shown in the lower segment of the image. The dashed line is $D_{s+p_x,y}(E) = \sum_{l=s,p_x,p_y} D_l(E)$ of the highest-energy structure (upper image segment) at the same x obtained using the $4 \times \sqrt{3}$ supercell (Figure 1). The inset in (e) shows the relative position of the scaled Fermi level $0 \leq \varepsilon_F \leq \Delta$ within the gap $\Delta(x)$ in $D_{s+p_x,y}(E)$ for the five structures.

these structures are characterized by the metallic p_z -derived band, with the Fermi level E_F falling in the gap $\Delta = \Delta(x)$ of the in-plane-derived density of states $D_{s+px,y}(E)$. For clarity, the relative Fermi level position $\varepsilon_F \equiv E_F - E_0$ within the gap Δ , with E_0 being the top of the filled $D_{s+px,y}(E)$, is plotted versus x in the inset of Figure 4e. This hallmark in the electronic spectrum has been shown⁹ to explain the stability of a few previously studied B layers. Figure 4 thus supports this stabilizing mechanism as being broadly applicable, including the here discovered family of almost isoenergetic phases of 2D boron. The geometries shown in Figure 4c,d constitute new ground-state structures of the planar B layer that are as stable as the α sheet⁹ but have higher x values.

It is interesting that the \square pattern in the lower image segment of Figure 4c ensures optimal mixing with the denser B_Δ , placing E_F approximately in the middle of Δ . To illustrate this effect, in the same panel we also plot $D_{s+px,y}(E)$ (dotted line) of the highest-energy structure (upper image segment) at the same $x = 1/8$ calculated with DFT using the $4 \times \sqrt{3}$ supercell (cf. Figure 1). This phase-separated $\square-\Delta$ configuration exhibits a considerable reduction in Δ .

In summary, we have combined DFT calculations with the CE method to explore the diversity of planar boron layers considered to be a $B_{1-x}\square_x$ pseudoalloy. As a result, we discovered a number of 2D stable polymorphs with nearly identical cohesive energies. Distinctly different in structure, they all lie in the rather narrow range of vacancy concentrations of 10–15%. This possibility of multiple structures/phases is in striking contrast to the other 2D materials: carbon displays well-known graphene structure with the only once discussed possibility of metallic pentaheptite.³⁸ Similarly, h-BN displays a distinct honeycomb structure³⁹ and no other known planar phases. For boron layers, the emerging picture is that, if ever synthesized (which is likely by chemical vapor deposition on a catalytic substrate or the thermal decomposition of borides similar to graphene formation from SiC^{40}), they will probably form coplanar patches of several polymorphs and thus will have a large degree of disorder. This contrasts with actively studied graphene, nitrides, and sulfides, making the further investigation of 2D boron particularly intriguing.

AUTHOR INFORMATION

Corresponding Author

*E-mail: biy@rice.edu.

Notes

The authors declare no competing financial interest.

ACKNOWLEDGMENTS

This work was supported by the Department of Energy, BES (grant no. ER46598). Computations were performed on TeraGrid under allocation TG-DMR100029 and the DAVinCI cluster acquired with funds from NSF grant OCI-0959097.

REFERENCES

- (1) Oganov, A. R.; Chen, J.; Gatti, C.; Ma, Y.; Ma, Y.; Glass, C. W.; Liu, Z.; Yu, T.; Kurakevych, O. O.; Solozhenko, V. L. *Nature* **2009**, 457, 863–867.
- (2) Ball, P. *Nat. Mater.* **2010**, 9, 6.
- (3) Huang, W.; Sergeeva, A. P.; Zhai, H.; Averkiev, B. B.; Wang, L. S.; Boldyrev, A. I. *Nat. Chem.* **2010**, 2, 202–206.
- (4) Kiran, B.; Bulusu, S.; Zhai, H. J.; Yoo, S.; Zeng, X. C.; Wang, L. S. *Proc. Natl. Acad. Sci. U.S.A.* **2005**, 102, 961–964.
- (5) Ciuparu, D.; Klie, R. F.; Zhu, Y.; Pfefferle, L. J. *Phys. Chem. B* **2004**, 108, 3967–3969.
- (6) Pfefferle, L.; Ciuparu, D. Growth of boron nanostructures with controlled diameter. EP Patent 1,695,392, 2006.
- (7) Oger, E.; Crawford, N. R. M.; Kelting, R.; Weis, P.; Kappes, M. M.; Ahlrichs, R. *Angew. Chem.* **2007**, 46, 8503–8506.
- (8) Szwacki, N. G.; Sadrzadeh, A.; Yakobson, B. I. *Phys. Rev. Lett.* **2007**, 98, 166804.
- (9) Tang, H.; Ismail-Beigi, S. *Phys. Rev. Lett.* **2007**, 99, 115501.
- (10) Yang, X.; Ding, Y.; Ni, J. *Phys. Rev. B* **2008**, 77, 041402.
- (11) Singh, A. K.; Sadrzadeh, A.; Yakobson, B. I. *Nano Lett.* **2008**, 8, 1314–1317.
- (12) Gopakumar, G.; Nguyen, M. T.; Ceulemans, A. *Chem. Phys. Lett.* **2008**, 450, 175–177.
- (13) Szwacki, N. G.; Sadrzadeh, A.; Yakobson, B. I. *Phys. Rev. Lett.* **2008**, 100, 159901.
- (14) Zhao, J.; Wang, L.; Li, F.; Chen, Z. J. *Phys. Chem. A* **2010**, 114, 9969–9972.
- (15) Li, H.; Shao, N.; Shang, B.; Yuan, L.; Yang, J.; Zeng, X. *Chem. Commun.* **2010**, 46, 3878–3880.
- (16) Prasad, D. L. V. K.; Jemmis, E. D. *Phys. Rev. Lett.* **2008**, 100, 165504.
- (17) De, S.; Willand, A.; Amsler, M.; Pochet, P.; Genovese, L.; Goedecker, S. *Phys. Rev. Lett.* **2011**, 106, 225502.
- (18) Wang, X.-Q. *Phys. Rev. B* **2010**, 82, 153409.
- (19) Sadrzadeh, A. et al. Unpublished data.
- (20) Sadrzadeh, A.; Pupyshcheva, O. V.; Singh, A. K.; Yakobson, B. I. *J. Phys. Chem. A* **2008**, 112, 13679–13683.
- (21) Özdoğan, C.; Mukhopadhyay, S.; Hayami, W.; Güvenç, Z. B.; Pandey, R.; Boustani, I. *J. Phys. Chem. C* **2010**, 114, 4362–4375.
- (22) Bezugly, V.; Kunstmann, J.; Grundkötter-Stock, B.; Frauenheim, T.; Niehaus, T.; Cuniberti, G. *ACS Nano* **2011**, 5, 4997–5005.
- (23) Xu, T. T.; Zheng, J. G.; Wu, N.; Nicholls, A. W.; Roth, J. R.; Dikin, D.; Ruoff, R. S. *Nano Lett.* **2004**, 4, 963–968.
- (24) Saxena, S.; Tyson, T. A. *Phys. Rev. Lett.* **2010**, 104, 245502.
- (25) Ding, Y.; Yang, X.; Ni, J. *Appl. Phys. Lett.* **2008**, 93, 043107.
- (26) Er, S.; de Wijs, G. A.; Brocks, G. J. *Phys. Chem. C* **2009**, 113, 18962–18967.
- (27) Kunstmann, J.; Quandt, A. *Phys. Rev. B* **2006**, 74, 035413.
- (28) Lau, K. C.; Pandey, R. *J. Phys. Chem. C* **2007**, 111, 2906–2912.
- (29) Sanchez, J. M.; Ducastelle, F.; Gratias, D. *Physica A* **1984**, 128, 334–350.
- (30) Hart, G. L. W.; Zunger, A. *Phys. Rev. Lett.* **2001**, 87, 275508.
- (31) Van der Ven, A.; Ceder, G. *Phys. Rev. B* **2005**, 71, 054102.
- (32) Mekata, M. *Phys. Today* **2003**, 56, 12–13.
- (33) Tang, H.; Ismail-Beigi, S. *Phys. Rev. B* **2010**, 82, 115412.
- (34) van de Walle, A.; Asta, M.; Ceder, G. *Calphad* **2002**, 26, 539–553.
- (35) Giannozzi, P.; Baroni, S.; Bonini, N.; Calandra, M.; Car, R.; Cavazzoni, C.; Ceresoli, D.; Chiarotti, G. L.; Cococcioni, M.; Dabo, I.; Dal Corso, A.; de Gironcoli, S.; Fabris, S.; Fratesi, G.; Gebauer, R.; Gerstmann, U.; Gougousis, C.; Kokalj, A.; Lazzeri, M.; Martin-Samos, L.; Marzari, N.; Mauri, F.; Mazzarello, R.; Paolini, S.; Pasquarello, A.; Paulatto, L.; Sbraccia, C.; Scandolo, S.; Sclauzero, G.; Seitsonen, A. P.; Smogunov, A.; Umari, P.; Wentzcovitch, R. M. *J. Phys.: Condens. Matter* **2009**, 21, 395502.
- (36) Perdew, J. P.; Burke, K.; Ernzerhof, M. *Phys. Rev. Lett.* **1996**, 77, 3865–3868.
- (37) Cabria, I.; Alonso, J. A.; López, M. *Phys. Status Solidi A* **2006**, 203, 1105–1110.
- (38) Crespi, V. H.; Benedict, L. X.; Cohen, M. L.; Louie, S. G. *Phys. Rev. B* **1996**, 53, 13303–13305.
- (39) Golberg, D.; Bando, Y.; Huang, Y.; Terao, T.; Mitome, M.; Tang, C.; Zhi, C. *ACS Nano* **2010**, 4, 2979–2993.
- (40) Sprinkle, M.; Ruan, M.; Hu, Y.; Hankinson, J.; Rubio-Roy, M.; Zhang, B.; Wu, X.; Berger, C.; De Heer, W. A. *Nat. Nanotechnol.* **2010**, 5, 727–731.
- (41) Li, F.; Jin, P.; Jiang, D.; Wang, L.; Zhang, S. B.; Zhao, J.; Chen, Z. J. *Chem. Phys.* **2012**, 136, 074302.

■ NOTE ADDED IN PROOF

Interestingly, one very recently suggested B₈₀ fullerene (structure 11 in Fig. 2 of Ref. 41), if unfolded, corresponds to one of the B-layers at $x=1/9$, uncovered in the present work.